Understanding the Impact of Upscaling THM Processes on Performance Assessment (DECOVALEX III BMT2)

First Draft Final Report from DOE/LBNL team

Hui-Hai Liu, Quanlin Zhou, Jonny Rutqvist, and Bo Bodvarsson

June 2002

Contents

1. Strategy

The major objective of Benchmark Test 2 (BMT2) is to quantitatively examine the reliability of estimates of repository host rock performance, using large-scale performance assessment (PA) models that are developed by upscaling small-scale parameters and processes. These small-scale properties and processes can be investigated based on either discrete-fracture-network (DFN) models or heterogeneous-porous-medium (HPM) models. While most research teams use DFN, we employ fractal-based HPM for upscaling purposes. Comparison of results based on fundamentally different approaches is useful for evaluating and bounding the uncertainties in estimating repository host rock performance.

HPM has both advantages and limitations when compared with DFN. DFM is conceptually more appealing because it explicitly describes fractures and the flow and transport processes that occur within them. However, HPM is more consistent with approaches used to derive field measurements of hydraulic properties (such as permeability). These properties are generally determined based on assumptions related to the continuum approach. HPM is also more straightforward in describing spatial-correlation structures of measured hydraulic properties. For example, potential flow features in the Borrowdale Vocanic Group (BVG) were found to show marked spatial clustering (Nirex, 1997), which is expected to result in a long range correlation in measured permeability distributions. This important behavior may not be captured with conventional DFNs, in which random distribution (or similar distributions) of individual fractures is assumed. The usefulness of HPM will be partially demonstrated in this report by a satisfactory description of the short interval testing data using Levy-stable fractals. (Recently, Jackson et al. (2000) also showed that equivalent HPMs could approximately describe flow processes within subgrid fracture networks.)

We use Monte Carlo simulations to determine flow and transport parameters at different scales. Since we have used a fractal-based approach supported by field measurements, effective properties will be scale-dependent. Effects of mechanical processes on flow and

transport properties will be also considered in the upscaling procedure. Then, large-scale thermal-hydrologic-mechanical (THM) and transport processes will be modeled.

2. Data Analysis

2.1 Short interval testing data

One difference between DFM and HPM is their need for different kinds of data as basic input. Because we use a HPM approach, we directly employ small-scale permeability data collected from the field rather than geometry data for different sets of fractures.

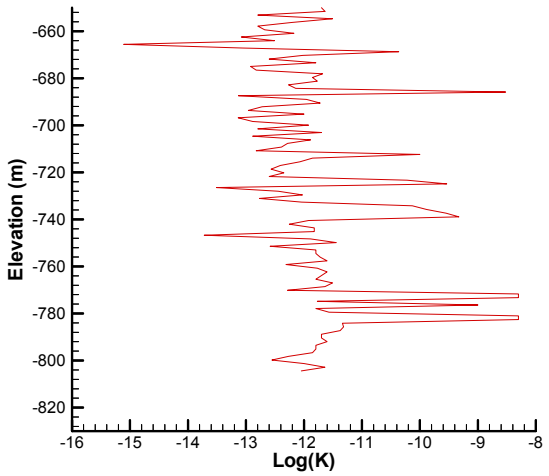

Figure 1. Conductivity distribution along a vertical borehole (RCF3) that were collected from the short interval testing

Figure 1 shows conductivity data collected from the short interval tests carried out in the Borrowdale Volcanic Group (BVG) (Nirex, 1997). The tests were conducted over a 156 m length interval and typically tested 1 to 2 m lengths of the borehole. They are comprised of 100 pulse injection tests and six production tests. In the definition of BMT2 (Version 4.0), the short interval testing data were considered to be collected from the upper formation (Near surface BVG). This may not be the case for the following two reasons. First, the largest permeability value inferred from the testing is about 3E-16 m^2 that is much smaller than the calibrated large-scale permeability 8.51E-14 m^2 for the upper formation. Second, in the Nirex report (page 4.13, 1997), the near-surface BVG formation was defined as the formation within 50 m of present day ground surface while

the total vertical testing interval is 156 m. Therefore, in this study we assume that the short interval testing data were collected from the lower formation (Fleming Hall Formation).

2.2 Fractional Levy motion

In this study, we first tested the usefulness of using Levy-stable fractals to characterize the short interval testing data. A number of researchers have used fractional Levy motion to characterize subsurface heterogeneities in porous media (Painter, 1996; Liu and Molz, 1997; Molz and Liu, 1997). While detailed discussions of fractional Levy motion can be found in those references, we provide here a brief introduction to Levy-stable distribution and parameters of fractional Levy motion (fLm).

Levy-stable distribution is a generalization of the well-known Gaussian distribution, given by

$$f(x) = \pi^{-1} \int_0^\infty \exp(-|Ck|^\alpha) \cos(kx) dk \qquad (1)$$

where α is the Levy index and C is the width parameter. The Levy stable distribution will be reduced to the Gaussian distribution for α =2. The width parameter C corresponds to the standard deviation of Gaussian distribution. Compared with Gaussian distribution, Levy distribution is characterized by long tails (Figure 2) and infinite theoretical second (and higher) moments. We further define increments of log(K), where K refers to conductivity (m/s), as

$$\Delta(h) = \log K(z+h) - \log K(z) \qquad (2)$$

where z is the spatial coordinate and h (m) is the lag. If log(K) distribution is consistent with fractional Levy motion, the probability distributions of log(K) increments for different lags follow Levy-stable distributions (Equation (1)) with the same Levy index and different width parameters given by

$$C(h) = C_0 h^H \qquad (3)$$

where C_0 and H are constants, with H representing the Hurst coefficient. It can be shown that Levy-stable fractals are self-similar at all scales (or lags). For $1/\alpha < H < 1$ positive increments tend to be followed by positive increments (persistence), while for $0<H<1/\alpha$

positive increments tend to be followed by negative increments (antipersistence). The latter is the case in this study.

H can also be considered as a measure of degree of long-range correlation. The larger the H value, the stronger the long-range correlation. If flow features were well connected, one would expect to observe relatively strong long-range correlation from the corresponding permeability measurements. Therefore, H values observed from permeability measurements could be used to approximately identify how well flow features are connected.

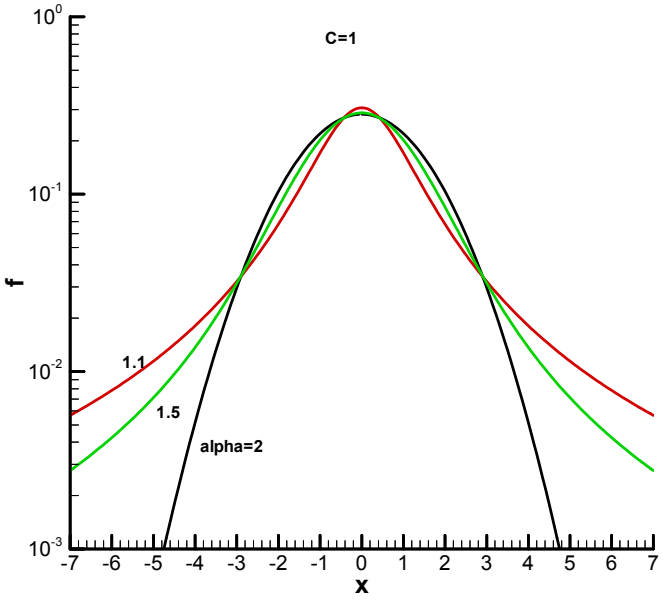

Figure 2. Levy-stable distributions with the same C value (C=1) and different Levy index (α) values. Note that α = 2 corresponds to the Gaussian distribution

The parameters characterizing fractional Levy motion include α, C, C_0, and H. To determine these parameters from the short interval test data, we used the quantile-based estimators for α and C for a given lag h (Fama and Roll, 1972; Painter, 1996). The scaling parameter H is calculated by fitting Equation (3) to the estimated C as a function of lag h.

2.3 Analysis Results

As an example, Figure 3 shows a comparison between a Gaussian distribution with variance determined from the data, a Levy-stable distribution with C and α values estimated from this study, and the observed probability density data for h = 1.56 m. Obviously, the Levy-stable distribution fits the data much better than the Gaussian distribution.

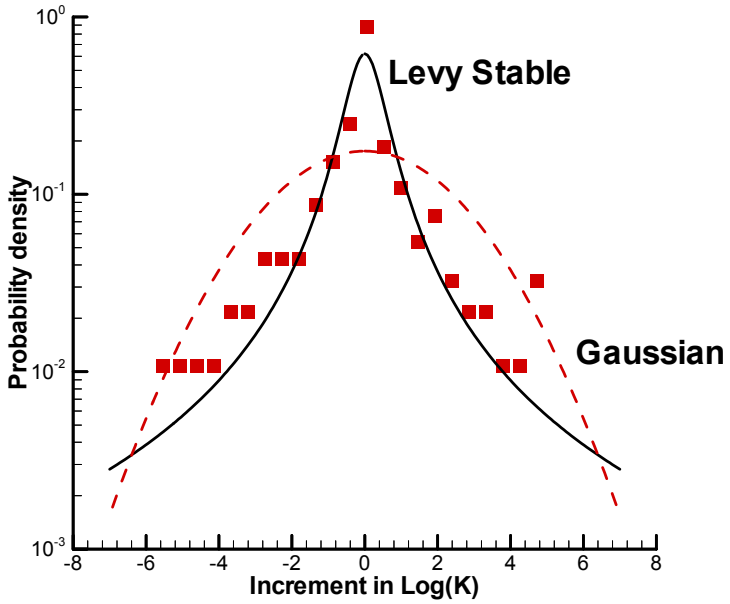

Figure 3. A comparison between a Gaussian distribution with variance determined from the data, a Levy-stable distribution with C and α values estimated from this study, and the observed probability density data for h=1.56 m

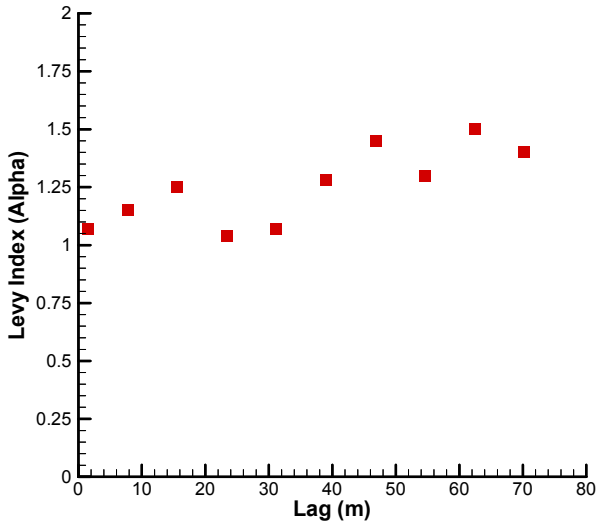

Figure 4. Estimated Levy index value as a function of lag

Figure 4 shows estimated α value as a function of the lags. Although estimated α values seem to exhibit a weak tread with lag, a constant α value (about 1.25) remains a good approximation for the estimates, a result supporting the usefulness of fractional Levy motion.

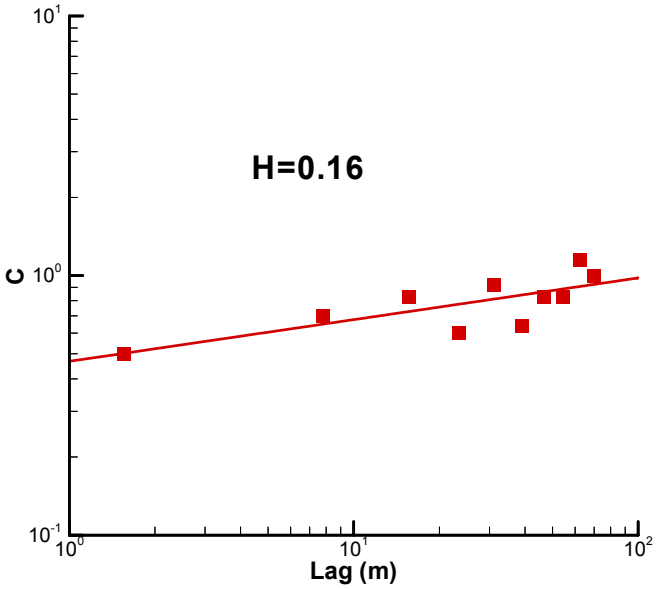

Figure 5. Levy width factor as a function of lags (Levy structure function)

Figure 5 shows the match of Equation (3) with C values estimated from the short interval testing data, indicating that a scaling relationship does exist at least on the scales up to 100 m. In summary, the analysis results (Figures 3-5) support the usefulness of fractional Levy motion in characterizing the spatial variability of measured conductivity. Table 1 gives the fLm parameter values estimated from the data and used for modeling studies described in other sections.

Table 1. The fLm parameter values estimated from the short interval testing data

Levy index (α)	Hurst Coefficient (H)	Parameter C_0 (Eq. (3))
1.25	0.16	0.47

2.4 Implications and Limitations of the Data Analysis

One important implication of our analysis is that long-range correlation exists in hydraulic property distributions. This is consistent with the field observation that PFFs are hydraulically significant and show marked spatial clustering. Capturing this behavior in an upscaling procedure is expected to be important. Also, because scaling behavior exists at least on scales up to 100 m, we can expect that the scale beyond which fractures can be represented by a homogeneous porous medium will be at least on the order of 100 m (if this scale exists).

Note that our analysis results are also supported by a number of studies reported in the literature. Based on observed data, Hirata (1987) and Yamamoto et al. (1993) found that fractures are not randomly distributed in space, but spatially clustered. The spatial clustering patterns could be described by fractals (Hirata, 1987; Yamamoto et al., 1993). Obviously, spatial clustering patterns of fractures should be closely related to spatial distributions of fracture permeability.

Nirex (1997) presented two conceptual models for flow within the BVG unit, corresponding to well-connected and unconnected flow feature clusters, respectively. As

previously indicated, Hurst coefficient, H, can be used to approximately identify how well flow features are connected. The relatively small H value (0.16), estimated from the short interval tests, seems to support the second conceptual model. This will be further discussed in Section 3.2.

In our analysis, we use only small-scale conductivity data and do not consider fracture geometry data. As a result, we are not able to consider the anisotropy resulting from fracture orientations. This may be resolved by incorporating anisotropy information from other teams using DFNs. Also, the small-scale conductivity data were collected from the lower formation of the reference problem. Similar data are not available from other formations. Given all this, we have to assume that fractal parameters developed from the short-interval test are applicable to all formations, while different mean hydraulic properties are used for different formations.

3 Modeling Approaches

This section presents an approach used to model large-scale flow and transport processes by combining a stochastic simulation of subsurface heterogeneity, upscaling rock properties, and a Monte Carlo simulation of flow and transport (Figure 6).

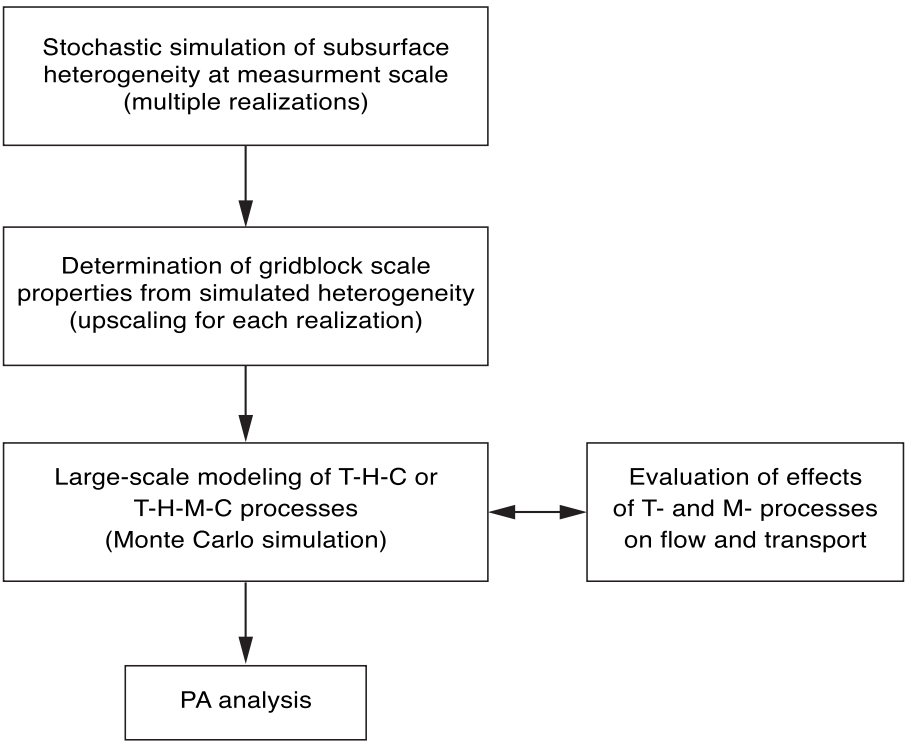

Figure 6. Adopted Modeling Procedure. PA refers to performance assessment.

3.1 Stochastic simulation of subsurface heterogeneity

Heterogeneous distributions of flow and transport properties are determined using stochastic simulations based on the fLm. The measurement scale associated with the short interval testing is assumed to be the average testing interval (1.56 m). Therefore, the heterogeneity is computationally generated with a gridblock size of 1.56 m × 1.56 m over the whole model domain, such that the resolution of generated heterogeneity is consistent with the measurement scale.

The fLm parameter values given in Table 1 are used for simulating log(k) distributions. Different formations are assumed to have the same fLm parameters except mean log(k) values, where k is permeability. The mean log(k) for the lower formation is considered to be the same as that calculated from the short interval testing data. The difference between mean log(k) value for the lower formation and the mean value for another formation is assumed to be the same as the corresponding log(k) difference between the two formations calculated from calibrated log(k) values given in Table 5.2 of Nirex

(1997) (see definition of BMT2). Table 2 gives the mean log(k) values used for stochastic simulations.

Table 2. Mean log(k) values for stochastic simulations

Rock Unit	Mean log(k)*
Upper Formation	-14.81
Fault Zone in Upper Formations	-14.31
Lower Formation	-18.98
Fault Zone in Lower Formation	-19.08

Note: k is permeability (m^2)

Because Levy-stable distributions have many novel and often unfamiliar properties, studies about generating fLm distributions are rare in the literature. As part of this study, we generalize a relatively simple and computationally efficient successive random additions (SRA) algorithm, originally developed for generating Gaussian fractals, to simulate fLm distributions. We also propose an additional important step in response to continued observations that the traditional SRA algorithm often generates fractal distributions with poor scaling and correlation properties. The generalized and modified SRA algorithm is validated through numerical tests; this work is reported elsewhere (Liu et al., 2001). This new algorithm is used for generating log(k) distributions.

3.2 Upscaling hydraulic conductivity

For large-scale modeling, numerical gridblock size ranges from 1.56 m × 1.56 m to 50 m × 50 m (see Section 2.5), while the gridblock size used for simulating heterogeneous log(k) distributions is 1.56 m × 1.56 m. In this case, upscaling (determination of effective parameters at numerical gridblock scales) is needed before performing large-scale modeling.

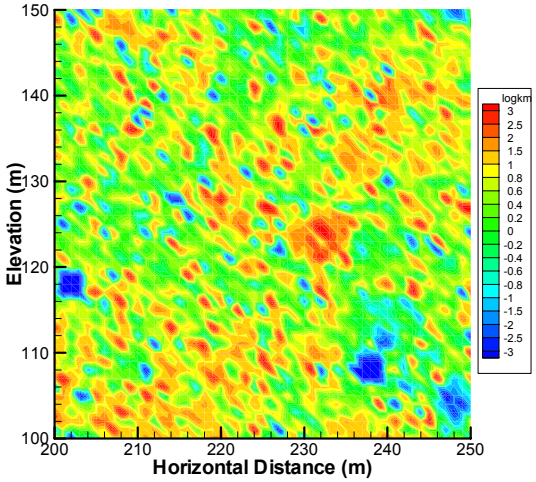

Figure 7. A numerical gridblock (for large-scale modeling) with subgrid log(k) heterogeneity that is simulated using fLm and has zero mean here. The elevation and horizontal distance correspond to global values in the large-scale model domain (Figure 8).

Figure 7 shows a numerical gridblock for large-scale modeling that contains subgrid heterogeneity simulated using the procedure discussed in Section 2.1. Different approaches are available for estimating gridblock-scale hydraulic conductivity (e.g., Renard and de Marsily, 1997). In this study, we use a simple numerical approach. For example, to determine effective horizontal hydraulic conductivity for a given numerical gridblock (Figure 7), we impose zero vertical flow conditions at the top and bottom boundaries and different hydraulic heads at the two side boundaries. Steady-state flow through the gridblock in the horizontal direction is then simulated. According to Darcy's law, the effective horizontal hydraulic conductivity is calculated as an average horizontal flux through a vertical line across the gridblock, divided by the hydraulic head gradient. A similar procedure can also be used to determine effective vertical hydraulic conductivity. For a given numerical mesh (e.g., Figure 17), values for gridblock-scale effective parameters (e.g., hydraulic conductivity and dispersivity) are automatically generated for each gridblock by a numerical code developed for this study. Table 2 shows Means and standard deviations for log of gridblock scale (50 m x 12.5 m) effective permeability for one realization of subsurface heterogeneity in large-scale model domain.

Table 2. Means and standard deviations for log of gridblock scale (50 m x 12.5 m) effective permeability for one realization of subsurface heterogeneity in large-scale model domain.

Formation	Mean	Standard Deviation
Upper	-14.8	1.13
Lower	-18.9	1.14

As previously indicated, the relatively small H value determined from the short interval tests seems to support a conceptual model that clustered flow features are not well connected globally. This is further confirmed by a good agreement between the mean and standard deviation of gridblock permeability from the lower formation (Table 2) with those for the upscaled permeability of the undifferentiated BVG unit, obtained by Nirex (Table 3.2, 1997) based on the conceptual model that flow features are not well connected.

3.3 Determination of transport parameters

Subgrid heterogeneity within a numerical gridblock for large-scale modeling may have an important effect on overall solute transport behavior. Therefore, this effect cannot be simply ignored. In this study, we use gridblock-scale dispersivity to approximately consider this effect.

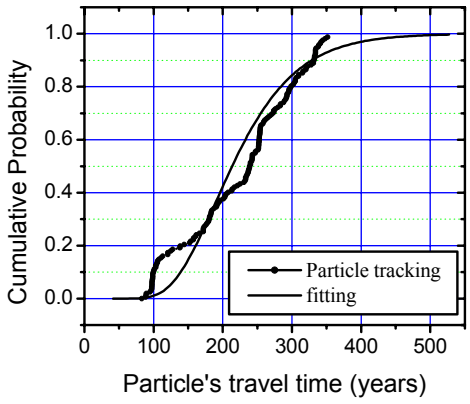

Figure 8. Fitting of numerically simulated breakthrough curve for a gridblock with an analytical solution (Domenico and Schwartz, 1990)

To numerically determine dispersivity values for each numerical gridblock for large-scale modeling, we introduce uniformly distributed solute particles at the inflow boundary for a given gridblock (Figure 8) after steady-state flow field is established. The flow boundary conditions are the same as those used for upscaling horizontal hydraulic conductivity (Section 2.2). Then, we use an analytical solution for one-dimensional solute transport to fit the simulated breakthrough curve by conceptualizing the gridblock as a "homogeneous" effective porous medium. The breakthrough curve is defined here to be the ratio of the number of solute particles transporting out of the gridblock at the outflow boundary, to the number of total particles initially introduced into the gridblock as a function of time. The algorithm of Zhou (1999) was used for the particle-tracking processes in which local-scale (mechanical) dispersion and molecular diffusion are ignored. The analytical solution used in this study is given as (Domenico and Schwartz, 1990):

$$\frac{C}{C_0} = \frac{1}{2} erfc\left[\frac{(x - vt)}{2(\alpha_L vt)^{1/2}}\right] \tag{4}$$

where C/C_0 is the relative concentration ranging from zero to one and corresponds to the cumulative probability in Figure 8 (v is the velocity, x is the horizontal length of the gridblock, t is the time and α_L is the longitudinal dispersivity). Note that for simplicity, we used dispersivity determined from the horizontal solute transport in a gridblock as the longitudinal dispersivity. The gridblock-scale transverse dispersivity is assumed to be zero.

Table 3. Means and standard deviations for log of gridblock scale (50 m x 12.5 m) dispersivity for one realization of subsurface heterogeneity in large-scale model domain.

Formation	Mean	Standard Deviation
Upper	5.1	9.5
Lower	5.0	9.8

3.4 Upscaling effects of mechanical process

3.4.1 Laboratory data and upscaling procedure

Mechanical processes in fractured rock can effect radionuclide transport through stress induced changes in porosity and permeability. A change in the three-dimensional stress field will act on pre-existing fractures, which will respond mechanically with associated changes in fracture aperture. Such stress-induced changes in fracture aperture may give rise to significant changes in the rock mass permeability, through a sensitive "cubic" relationship between fracture aperture and fracture flow. Thus, to investigate the effects of mechanical processes on transport, we must analyze the impact of stress on permeability of the fracture rock mass and the upscaling of the relationship between stress and permeability from available lab-scale data.

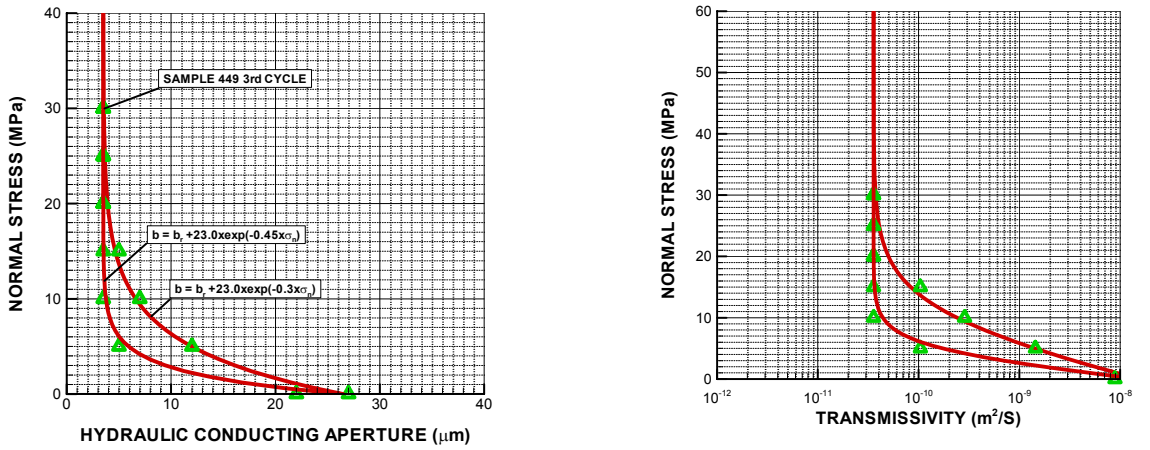

(a) **(b)**

Figure 9. (a) Exponential stress vs. aperture function fitted to experimental results on sample 449 and (b) corresponding stress versus transmissitivity relationship

In this study the upscaling of the mechanical processes (or essentially the stress-permeability relationship) is conducted in a similar manner to that for the previous analysis of hydraulic processes. In Section 2.2, hydraulic properties were upscaled from the basic 1.56 meters block scale—corresponding to the packer separation of small scale pumping tests—to each grid block of the model domain by a stochastic flow analysis. For studying the effects of mechanical processes, a stress-permeability relationship will be

added to the analysis at the 1.56 m block level, and derived for the final gridblocks through the stochastic flow analysis. If significant, upscaled relationships will be included in the final large-scale coupled THM simulation of BMT2.

A small-scale stress-permeability relationship is obtained from the few available laboratory tests on single fractures. First, the basic stress versus aperture function is fitted to observed laboratory results according to one example in Figure 9a. The function used is:

$$b = b_r + b_m = b_r + b_{\max} \exp(-\alpha' \sigma \ ) \quad (5)$$

where b is total hydraulic aperture, b_r is hydraulic residual aperture, b_m is "mechanical aperture", b_{max} is the maximum "mechanical aperture", α' is a parameter related to the curvature of the function, and σ is the normal stress across the fracture. Second, the basic stress-aperture relationship can be translated into a stress-transmissivity relationship (Figure 9b), which then is deduced to be a stress-permeability relationship for the 1.56 m block size.

Figure 1 shows that 1.56-m transmissivities varies over 7 orders of magnitude, with most values around 1.0e-13 to 1.0e-12 m^2/s. Assuming a homogenous porous media and 1.56 meters packer spacing such transmissivity values yields permeabilities of 6e-21 m^2 and 6e-20 m^2, respectively. These values are equivalent to intact rock permeability values indicating that no permeable fractures are intersecting the borehole in those test sections. For Sample 446 in Figure 9b, at normal stress level corresponding to the depth of the packer tests—about 18 to 25 MPa—the fracture transmissivity is on the order of 10^{-11} to 10^{-10} m^2/s. Thus, transmissivities above 10^{-11} in Figure 9b are likely to be dominated by flow in one or several intersecting fractures, and most probably dominated by flow in one fracture or one flow channel in a fracture plane. Table 4 gives parameters for equivalent smooth-wall conducting apertures obtained from 4 samples (Samples 229, 449, 5 and 7) (Definition of BMT2, Version 5)

Table 4, Aperture properties related to the mechanical process for the four samples.

Average b_r	5.5E-6 m
Standard deviation of b_r	1.91E-6 m
Average b_{max}	15 E-6 m
Range of b_{max}	10 to 23 E-6 m
Average $R_b=b_r/b_{max}$	0.40

The upscaling of the stress-permeability relationship from 1.56 m scale to relevant gridblock scale is conducted through a stochastic simulation of stress and fluid flow through a heterogeneous domain (Figure 10). The initial permeability field is generated from the fLm according to Section 2.1. Then a stress change is induced and a new flow simulation is conducted to derive a new effective permeability. For simplicity, we use a single stress-permeability relationship for both loading and unloading conditions. An average α' value (0.38) is used for stress-permeability relationship at the 1.56 m scale.

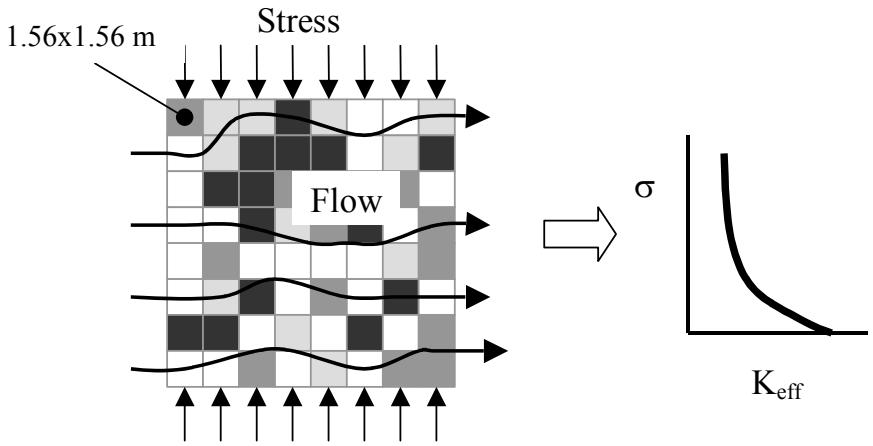

Figure 10. Outline of stochastic stress and fluid flow analysis for studying the upcaling of the 1.56 m stress-permeability relation

An important step for upscaling the stress-permeability relationship is to relate local permeability (at 1.56 m scale) to parameters b_r, b_{max} and fracture frequency f. We assume

that at the 1.56 m scale, local permeabilities can be considered to result from horizontal and vertical fractures. Different assumptions regarding relations among local permeability and the relevant parameters (f, b_r, and b_{max}) will give rise to different upscaling models. In this report, we present two useful models.

3.4.2 Upscaling Model I

Local permeability variation is expected to result from both f and aperture variations. In this model, we assume that all the fractures are identical and the permeability variation is purely due to changes in fracture frequency f. The relation among fracture aperture, frequency and local permeability k_L is (CRWMS M&O, 1999):

$$b = (\frac{12k_L}{f})^{1/3} \qquad (6)$$

Combining Equations (5) and (6) gives

$$\frac{k_L(\sigma_{in}, \Delta\sigma)}{k_L(\sigma_{in})} = \left(\frac{b}{b_{in}}\right)^3 = \left[\frac{R_b \exp(\alpha'\sigma_{in}) + \exp(-\alpha'\Delta\sigma)}{R_b \exp(\alpha'\sigma_{in}) + 1}\right]^3 \qquad (7)$$

where σ is the (effective) normal stress (MPa), subscript "in" refers to the initial (in-situ) conditions, and Δσ is the stress change ($\sigma - \sigma_{in}$). Since all the fractures are assumed to be identical, R_b will be a constant through the model domain.

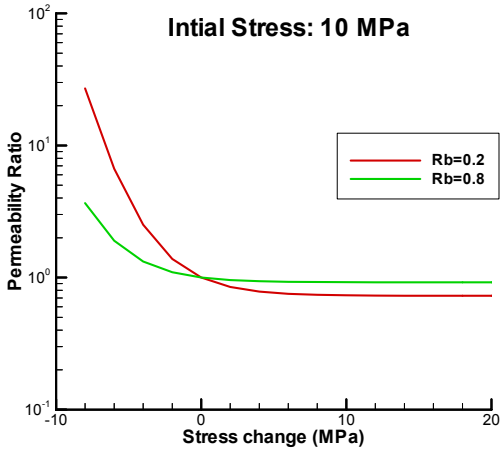

Figure 11. Local-scale stress-permeability relationships (Model I) for two different R_b values.

It is important to note that local permeability ratio (Equation (7)) does not depend on local permeability and frequency. Therefore, the same relation is also valid for effective permeability (K_{eff}) ratio at a gridblock scale:

$$\frac{k_{eff}(\sigma_{in},\Delta\sigma)}{k_{eff}(\sigma_{in})}=\left[\frac{R_b\exp(\alpha'\sigma_{in})+\exp(-\alpha'\Delta\sigma)}{R_b\exp(\alpha'\sigma_{in})+1}\right]^3 \qquad (8)$$

In other words, the permeability ratio is not scale-dependent in this model and numerical upscaling procedure is not needed. For a given initial stress and a stress change, the permeability ratio is purely determined by the parameter R_b. A large R_b corresponds to a large portion of residual aperture (b_r) in the total aperture b, and therefore gives rise to relatively weak response to mechanic process (Figure 11). The average R_b value from the four lab measurements is given in Table 4.

3.4.3 Upscaling Model II

While Model I gives a simple, closed-form stress-permeability relation at gridblock scale, it is not consistent with field observations from the unsaturated zone of Yucca Mountain, showing that the permeability ratio depends on local permeability. A smaller initial local permeability generally corresponds to a larger permeability ratio. Motivated by this observation, we develop the second model by assuming that there are single vertical and horizontal fractures within a 1.56m x 1.56m block. The permeability variation is assumed to be due to b_r variation while b_{max} is fixed (b_{max} = 23E-6 m for the upper formation and 10E-6 m for the lower formation). The b_{max} values for the two formations correspond to the largest and smallest b_{max} values observed from the lab measurements (Table 4).

Numerical upscaling procedure described in Section 3.4.1 is used for a 50 m x 50 m gridblock containing a heterogeneous permeability distribution characterized by Levy fractal. Within a 1.56 m x 1.56 m block, the initial aperture is calculated from Equation (6) with the corresponding local permeability. Then b_r at that small block is calculated from Equation (5) for a given initial stress. Note that Equation (7) is still valid for local

scale permeability ratio, but Equation (8) does not hold for the 50 m x 50 m gridblock. This is because R_b is not constant anymore.

Figure 12 shows local permeability ratio calculated with the method described above. It increases with describing initial local permeability, which is consistent with observations from Yucca Mountain. Because b_{max} is fixed, a smaller initial permeability will give a smaller b_r or a smaller R_b. Based on Equation (7), this corresponds to a smaller permeability ratio.

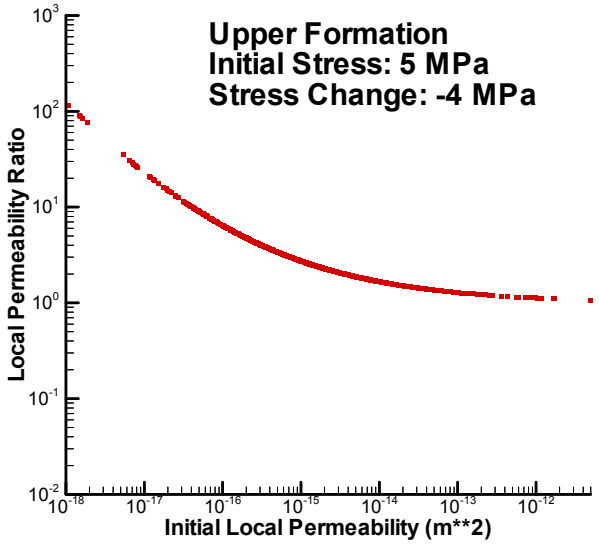

Figure 12. Ratio of local permeability within the 50 m x 50 m gridblock as a function of initial local permeability. Local scale is defined as the scale corresponding to 1.56 m x 1.56 m block.

For a given mean log(k) for the 1.56 m x 1.56 m blocks within the 50 m x 50 m gridblock, we can simulate effective permeability ratio for the gridblock for different initial stresses and stress changes. Based on Equations (5) and (6), the local scale R_b is given by

$$R_b = \left(\frac{k_L(\sigma_{in})}{k^*} \right)^{1/3} - \exp(-\alpha' \sigma_{in}) \qquad (9\text{-}1)$$

$$k^* = \frac{b_{\max}{}^3 f}{12} \qquad (9\text{-}2)$$

Numerical experiments indicate that simulated stress-effective permeability relations can be approximately represented by Equation (8) with an effective parameter R_b* :

$$\frac{k_{eff}(\sigma_{in},\Delta\sigma)}{k_{eff}(\sigma_{in})}=\left[\frac{R_b^{\,*}\exp(\alpha'\sigma_{in})+\exp(-\alpha'\Delta\sigma)}{R_b^{\,*}\exp(\alpha'\sigma_{in})+1}\right]^3 \qquad (10)$$

Numerical experiments also indicate that the effective parameter R_b* can be approximated by a modified from of Equation (9):

$$R_b^{\,*}=\left(\frac{k_{eff}(\sigma_{in})}{k^*}\right)^{1/3}-\exp(-\alpha'\sigma_{in}) \qquad (11)$$

As an example, Figure 13 shows a comparison between results calculated from Equation (10) with numerical simulation results (data points). A good agreement is obtained.

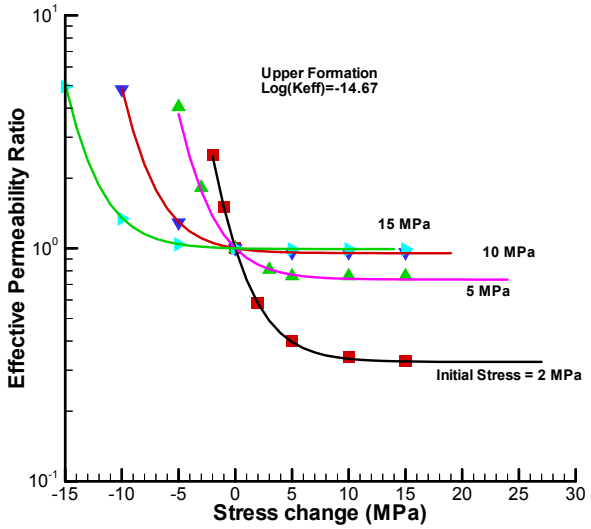

Figure 13. a comparison between results calculated from Equation (10) with numerical simulation results (data points).

For the lower formation, we consider fractures with initial aperture smaller than 1.7E-6 m to be a part of the matrix that is assumed not to respond to stress change. The aperture value of 1.7E-6 is determined as the mean of measured residual aperture minus twice of its standard deviation (Table 4). This treatment is motivated by the observation that in the

Short Interval Tests, "for intervals not crossed by an identified PFF, the effective permeability determined from the tests is consistent with the permeability of the matrix in BVG (determined from measurements on cores)" (Page 4.14, Nirex, 1997).

3.4.4 Additional Remarks

Two models are developed for calculating gridblock-scale stress-permeability relationships. Although Model I is developed by assuming identical properties for individual fractures and spatially variable fracture densities, it can be mathematically shown that the model is also valid for individual fractures with different aperture parameters (e.g., b_r and b_{max}) as long as R_b is the same for individual fractures. For the given parameter values for the problem under consideration, Model I generally predicts larger permeability changes due to mechanical processes (Figure 14).

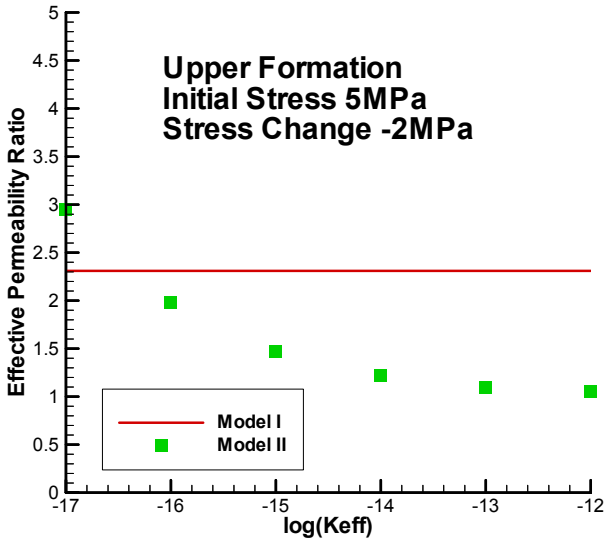

Figure 14. Comparison of permeability change due to mechanical process as a function of $\log(K_{eff})$ for the 50 m x 50 m gridblock.

Another interesting finding from this upscaling exercise is that local permeability ratio purely depends on R_b for a given initial stress and a stress change. R_b is an important parameter to characterize effects of the mechanic process on hydraulic properties. Effective R_b for large-scale stress-permeability relationships, R_b*, seems to exist. How to

relate R_b (or R_b*) to local (or large-scale) permeability is of interest for modeling M-H processes, and deserves further studies.

3.5 Large-scale modeling: Monte Carlo simulations

Figure 15 shows a numerical grid used for large-scale modeling studies. A very fine discretization (in both vertical and horizontal directions) is used near the repository, such that subsurface heterogeneity can be better represented and detailed flow and transport behavior can be simulated in that area.

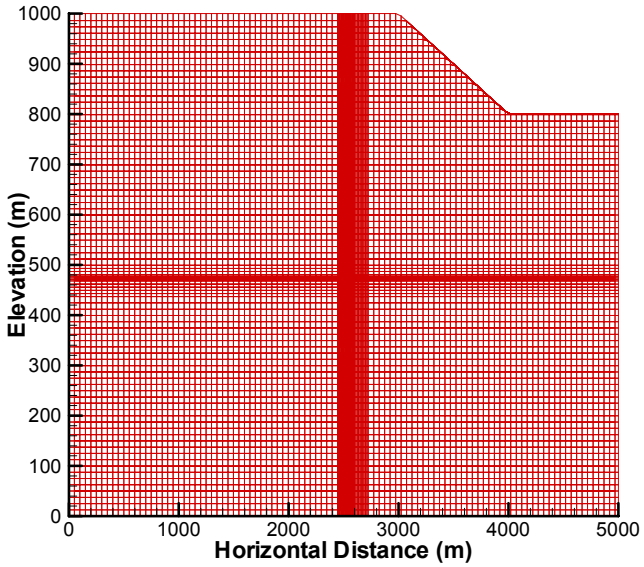

Figure 15. Numerical grid

Following the problem definition of BMT2 (Versions 5.0 and 6.0), the base and sides of the grid are no water-flow boundaries. Water table is at the ground surface. The air temperature at sea level is assumed to be constant at 11^0C. For ground surfaces above sea level, the adiabatic laps is 6.2^oC/km. Sea temperature is a constant at 11^0C. Basal heat flow is 54 mW/m^2. No heat flow is assumed through the sides of the large-scale model. After steady-state TH processes are achieved under ambient conditions, heat source at repository is introduced. The repository is assumed to contain 60 canisters of HLW uniformly distributed over a horizontal repository of 100 m x 100m (Definition of BMT2 (version 6.0)). For the two-dimensional problem under consideration, heat flux from the

repository is calculated as heat flux from a single canister, multiplied by 60 (number of canisters) and divided by 100 m. This treatment implies that the width of the 2D-model domain in the third direction (perpendicular to the 2D domain) is 1 m. Solute mass is released from the center of the repository with a permeability of 5.0E-21 m^2.

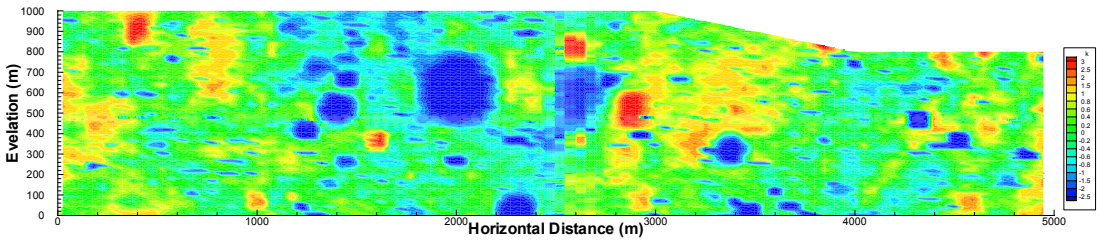

Figure 16. Distribution of difference between gridblock-scale log(k) and mean log(k) for the corresponding formation. Here k refers to horizontal hydraulic conductivity.

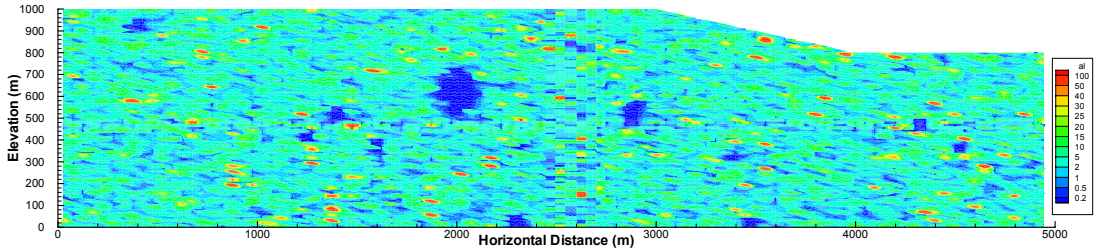

Figure 17. Distribution of gridblock-scale longitudinal dispersivity

Since significant heterogeneity still exists for gridblock-scale properties (Figures 12 and 13), Monte Carlo simulation is needed for evaluating flow and transport processes. Figures 16 and 17 correspond to one realization of subsurface heterogeneity only. Multiple realizations of subsurface heterogeneity are employed to determine the mean flow and transport processes and the associated uncertainties. The numerical code T2R3D (Wu et al., 1996) is used to simulated coupled TH and tracer transport processes.

4. Large-scale Modeling Results: Sensitivity Studies

4.1 Effects of Thermal Process

Simulations are performed to evaluate effects of heat released from the repository on radionuclide transport process. The hydraulic property distributions presented in Figures 16 and 17 are employed in these simulations.

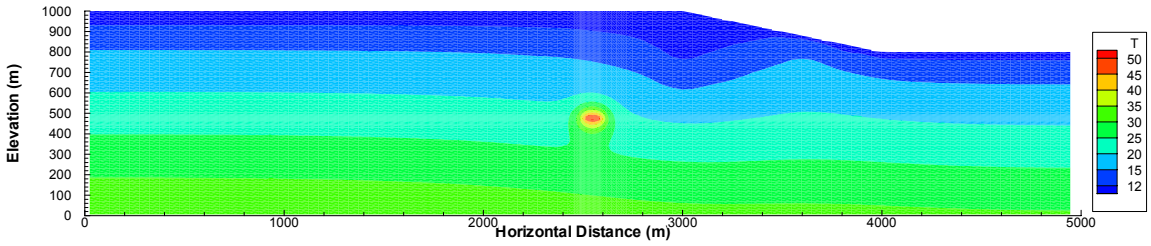

Figure 18. Temperature distribution at 100 years after the repository starts to release heat.

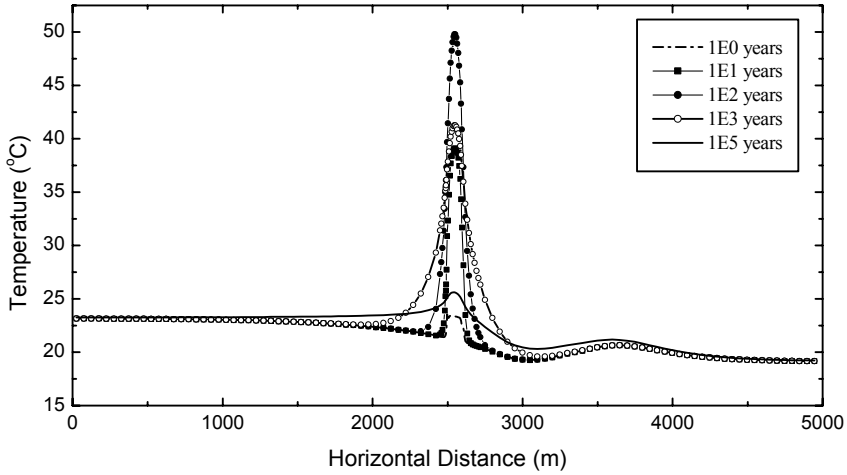

Figure 19. Temperature distribution along the horizontal line cross the repository

Figure 18 shows temperature distribution at 100 years after the repository starts to release heat. The temperature contours near ground surface and sea become relatively curved for horizontal distances between 2,400 and 4,000 m. This is a signature of relatively large

downward water flux at and near ground surface for horizontal distances between 2,400 and 3,000 m, partially resulting from relatively large permeabilities in that area (Figure 16). This also reflects relatively large upward water flux to the sea for the horizontal distances between 3,000 and 4,000 m. Figure 19 shows a temperature distribution along a horizontal line across the repository as a function of time. The highest temperature at the repository of about 50 ^{o}C is reached in about 100 years.

Tracer transport simulations, coupled with TH processes, are performed for cases with and without considering heat released from the repository. Figure 20 shows a tracer concentration distribution at 100 million years for the case considering heat released from the repository. Figure 21 compares breakthrough curves at a perimeter surface at 50 m from the boundary (wall/floor/roof) of the repository. They correspond to cases that do and do not consider heat release from the repository, respectively. As shown in Figure 21, the differences between the two curves are small, indicating that the heat release has an insignificant effect on near-field radionuclide transport. Since heat release mainly affects the temperature distribution near the repository (Figures 18 and 19), it is expected that the heat release has an even more insignificant effect on far-field radionuclide transport. Therefore, the effects of the heat release on radionuclide transport may be negligible for the problem considered.

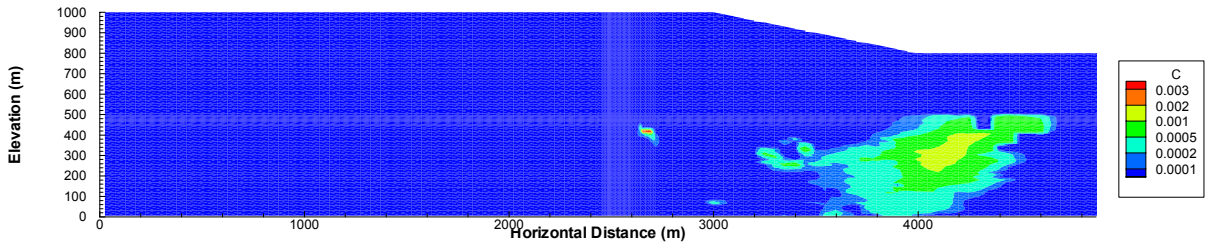

Figure 20. Relative tracer concentration distribution at 100 million years, simulated without considering heat released from the repository. The relative concentration is defined as tracer concentration divided by the initial tracer concentration at the repository.

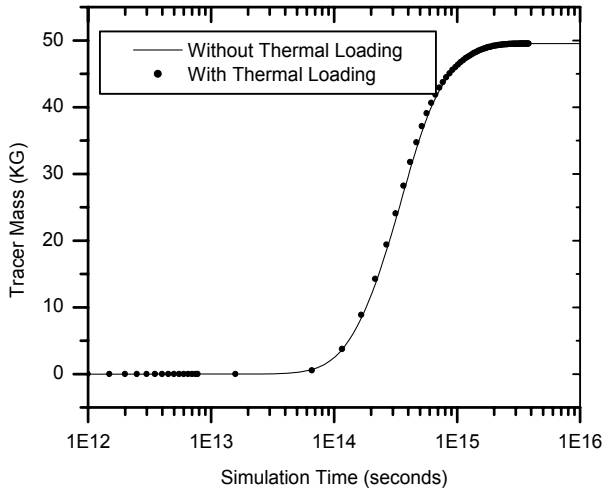

Figure 21. Accumulative tracer mass transporting across a perimeter surface at 50 m from the boundary of the repository. The initial tracer mass at the repository is 50 kg.

4.2 Effects of Thermal-Mechanical (TM) Process

An estimate of thermomechanically induced permeability changes is conducted for the case of mean permeability values consistent with those given in Table 2. In this case, we are using the 50-meter scale stress-permeability relationships developed in Section 3.4.1 using upscaling Method I and II. Figure 22 presents the permeability as function of an isotropic effective stress (left vertical axis) or as a function of corresponding approximate depth (right vertical axis). The figure shows that the 50-meter permeability relationship is more sensitive to stress changes for upscaling Method I. At the level of the repository (about 500 meters depth) the stress is so high that fracture are almost complete compressed mechanically and the permeability (for both Method I and II) is approaching its residual value. Therefore, a further stress increase due to thermal stresses cannot significantly reduce the permeability further. If, on the other hand, the rock is unloaded (for example due to excavation), the permeability could theoretically increase by up to 2 orders of magnitude (for Method I). Also note that the mean initial permeability in

Formation 1 (lower formation) is less than the cut-off values for matrix permeability and is therefore considered to be independent of stress.

For simplicity, the simulation is conducted starting at an initial depth-dependent permeability distribution according to Figure 22. The 100 by 10 meters repository area is represented by a heat source while no rock material is removed from the model (to avoid collapse of the overlying rock). The thermal stresses and associated permeability changes were calculated at 100 years and 1000 years for a thermal expansion coefficient of $1 \cdot 10^{-5}$ $°C^{-1}$. Although, the temperature reaches its maximum of 50°C at about 100 years (Figure 21), most changes in the permeability field occurs at 1000 years when the heat transfer occurs in a larger area around the repository. At 1000 years, the thermal stress near the repository increases by about 10 to 20 MPa with most changes taking place in the horizontal direction. In the vertical direction, smaller thermal stresses are induced due to the horizontal elongation of the repository area, and its proximity to the free land surface. As a consequence of higher thermal stress in the horizontal direction, most changes in permeability occur in the vertical permeability. A small reduction in permeability occurs above the repository between 100 to 500 meters depth. Such reduction is possible because the location on the stress permeability function above the residual permeability value. At the ground surface, the stresses horizontal stresses are reduced and as a consequence the vertical permeability increases by a factor of 2.6. The permeability changes in Figure 23 are calculated using upscaling model I. For model II, the permeability changes are much smaller.

This simulation indicates that the thermomechanically induced permeability changes are relatively small. However, the estimated permeability changes are very depended on the applied stress-permeability function. In this case, the stress permeability functions were developed using laboratory scale data, which was directly applied to the 1.56 meters block scale. Many in situ experiments have indicated that the hydromechanical properties are different in situ then corresponding laboratory properties. For example, b_{max} can be considerable larger for a larger fracture surface area and b_r may also be different.

Therefore, a sensitivity study should be conducted considering possible difference between laboratory and in situ hydromechanical properties.

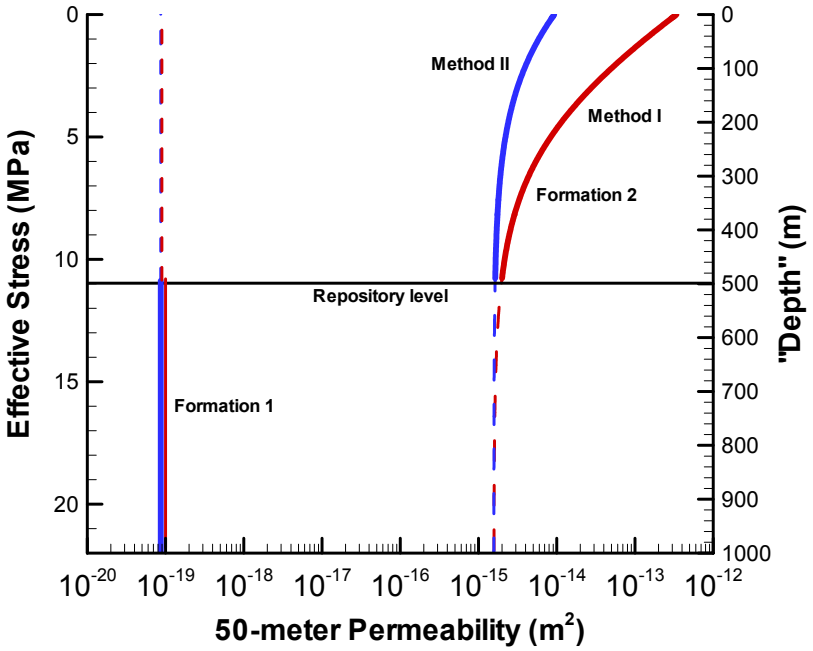

Figure 22. 50-meters scale permeability as a function of effective stress (right hand vertical axis) and approximate "depth" (left hand vertical axis) for upscaling Model I (red lines) and Model II (blue lines).

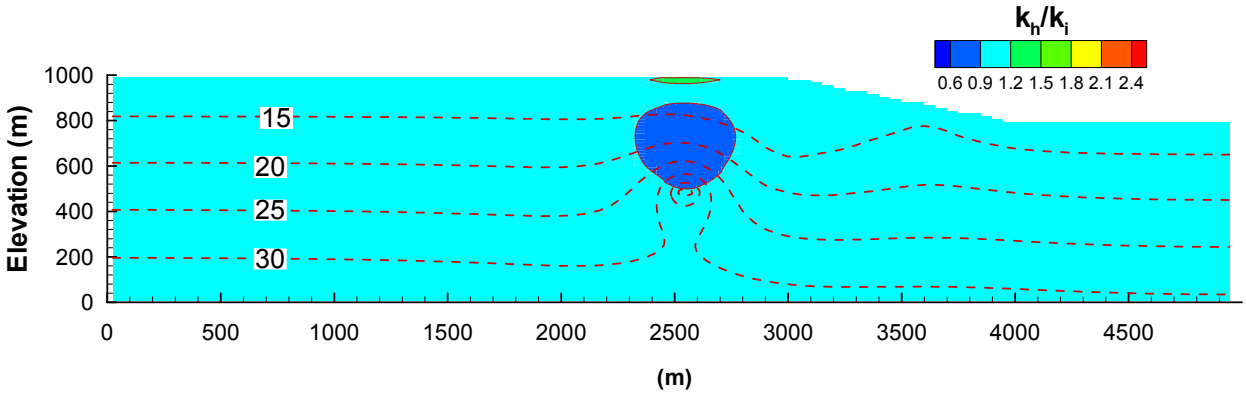

(a)

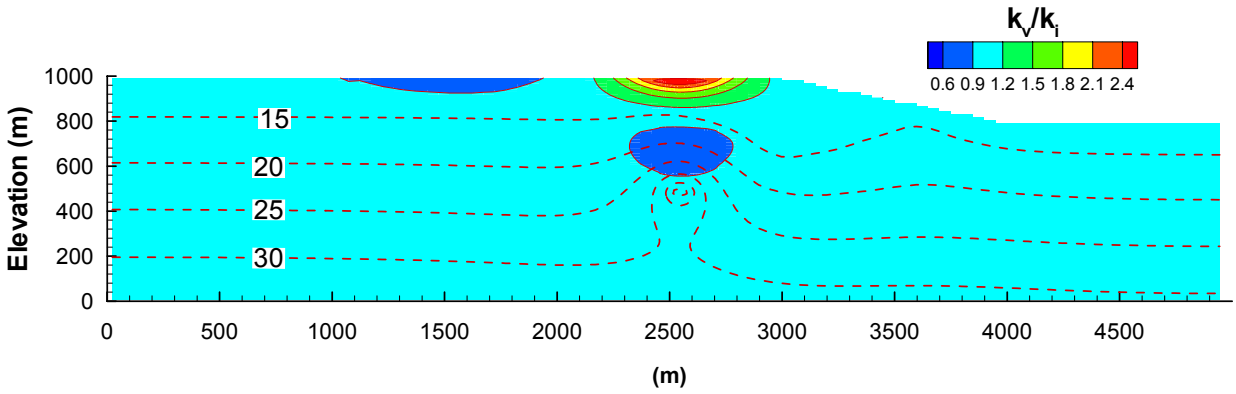

(b)

Figure 23. Thermomechanically induced changes in (a) horizontal permeability and (b) vertical permeability at 1000 years. Dashed contour lines are temperature isotherms.

4.3 Effects of Fracture Porosity

In the large-scale preliminary simulations discussed above, a measured porosity of 5.7% for core samples collected from the upper formation is used. This porosity corresponds to the matrix porosity and can be considered as the upper limit of fracture porosity. To evaluate effects of fracture porosity on solute transport, we compare simulation results with the porosity of 5.7% and fracture porosity values estimated based on an approach similar to that used by CRWMS M&O (2000). The permeability distribution used in this section is the same as that given in Figure 16.

For the purpose of estimating fracture porosity, we assume that fracture networks to consist of infinite fractures in vertical and horizontal directions. The total fracture frequency can be estimated by

$$f = \sum_i \frac{1}{S_i} \quad (9)$$

where S_i is average fracture spacing for fracture set i. Then for a two-dimensional fracture network, fracture porosity is calculated by

$$\phi_f = 2bf \quad (10)$$

where b is hydraulic aperture calculated with Equation (6). CRWMS M&O (2000) showed that fracture permeabilities calculated using hydraulic aperture are much smaller than those determined from gas tracer data, while the latter were considered to be more reliable. Therefore, fracture porosities calculated using (10) probably represent lower limits of fracture porosities. Table 5 gives calculated fracture porosities using Equation (10) for the upper and lower formations.

Table 5. Calculated fracture porosities using Equation (10)

Formation	Fracture Porosity
Upper Formation*	2.8E-4
Lower Formation*	1.64E-5

*Including Faults

Figure 24 compares simulated breakthrough curves cross a perimeter surface at 50 m from the boundary of the repository for different porosities.

Porosity values from Table 5 yields a much shorter breakthrough time, indicating that fracture porosity has a significant effect on the performance of potential repository when the matrix diffusion is ignored.

In the simulations shown in Figure 24, thermal loading is considered. To further evaluate the thermal loading on near-field radionuclide transport for porosity values given in Table 5, Figure 25 compares breakthrough curves with and without thermal loading at a perimeter surface at 50 m from the boundary of repository. The thermal loading has a noticeable, but insignificant effect on radionuclide transport. (Thermal loading results in slightly shorter tracer travel times.) This is consistent with our discussion in Section 4.1.

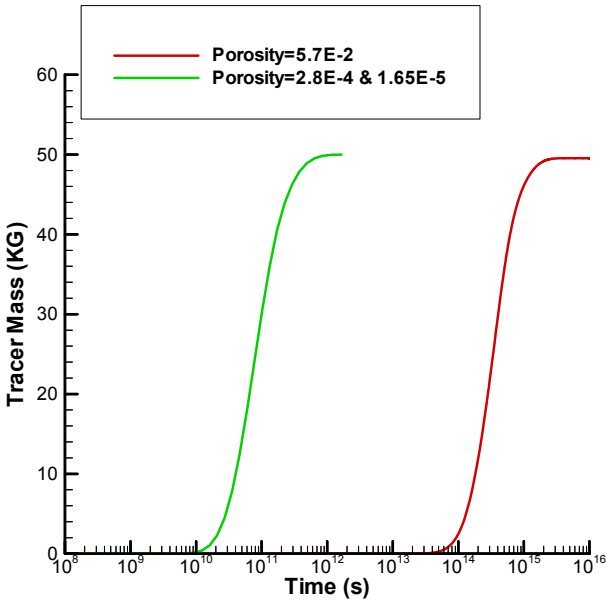

Figure 24. Accumulative tracer mass transporting across a perimeter surface at 50 m from the boundary of the repository for different porosity values. The initial tracer mass at the repository is 50 kg.

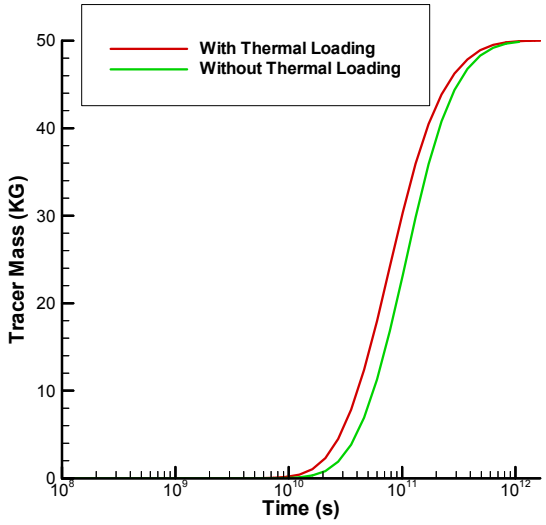

Figure 25. Accumulative tracer mass transporting across a perimeter surface at 50 m from the boundary of the repository. The initial tracer mass at the repository is 50 kg.

5. Summary

Analysis of the short interval testing data indicates that the spatial variability of measured conductivity is well characterized by fractional Levy motion. The long-range correlation of measured conductivity suggests that the scale (above which fractures can be represented by a homogeneous medium) be at least on the order of 100 m (if this scale exists).

A modeling approach (combining stochastic simulation of subsurface heterogeneity, upscaling rock properties, and Monte Carlo simulation of flow and transport) is presented. Numerical codes to generate fLm distributions and to automatically determine gridblock-scale effective properties have been developed for this study. Two models for upscaling stress-permeability relations are also developed.

Our preliminary simulation results, obtained by considering coupled thermal, hydraulic and tracer transport processes, indicate that the heat release does not have an insignificant effect on radionuclide transport, but fracture porosity does. The T-M processes due to the thermal loading may not result in significant changes in permeability distributions.

References

CRWMS M&O, Analysis of Hydrologic properties data, Las Vegas, Nevada, 2000.

Fama, E., and R. Roll, Parameter estimates for symmetric stable distributions. J. Am. Stat. Assoc., 66, 331, 1972.

Hirata,T., T. Saton and K. Ito, Fractal structure of spatial distribution of micro fracturing in rock, Geophys. J. R. Abstr. Soc., 90,369-374, 1987.

Jackson, P. C., A. R. Hoch, and S. Todman, Self-consistency of a heterogeneous continuum porous medium representation of a fracture continuum, Water Resources Research, 36(1), 189-202, 2000.

Liu, H. H., and F. J. Molz, Comment on "Evidence for non-Gaussian scaling behavior in heterogeneous sedimentary formations" by Scott Painter, Water Resources Research, 33(4), 907-908, 1997.

Liu, H.H., G.S. Bodvarsson, F.J. Molz and S. Lu, A generalized successive random additions algorithm for simulating fractional Levy motion. Water Resources Research (in review), 2001.

Molz, F.J., and H. H. Liu, Fractional Brownian motion (fBm) and fractional Gaussian noise (fGn) in subsurface hydrology. Water Resources Research, 33(10), 2273-2286, 1997.

Pinter, S, Evidence for non-Gaussian scaling behavior in heterogeneous sedimentary formations, Water Resources Research, 32(5), 1183-1195, 1996.

Renard, Ph., and G. de Marsily, Calculating equivalent permeability: A review, Adv. Water Resour., 20(5-6), 1997.

United Kingdom Nirex Limited, An Assessment of the post-closure performance of a deep waste repository at Sellafield, Science Report S/97/012, 1997.

Wu, Y. S., C.F., Ahlers, P., Fraser, A., Simmons, K., Pruess, Software qualification of selected TOUGH2 modules. LBNL-39490, Lawrence Berkeley National Laboratory, Berkeley, CA, 1996.

Yamamoto, H., K. Kojima and H. Tosaka, Fractal clustering of rock fractures and its modeling using cascade process, in Scale Effects in Rock Masses 93 (Edited by Pinto da Cunha), Balkema, Rotterdam, 1993.

Zhou Q., Modeling Seawater intrusion in coastal aquifers, Ph.D. thesis, Israel Institute of Technology, Haifa, Israel.

Acknowledgment. We are indebted to Guoming Li and Dan Hawkes at Lawrence Berkeley National Laboratory for their critical and careful reviews of a preliminary version of this manuscript. This work was supported by the Director, Office of Civilian Radioactive Waste Management, U.S. Department of Energy, through Memorandum Purchase Order EA9013MC5X between Bechtel SAIC Company, LLC, and the Ernest Orlando Lawrence Berkeley National Laboratory (Berkeley Lab). The support is provided to Berkeley Lab through the U.S. Department of Energy Contract No. DE-AC03-76SF00098.